Supporting Information

Selective Conversion of CO_2 to CH_4 Enhanced by WO_3/In_2O_3 S-scheme Heterojunction Photocatalyst with Efficient CO_2 Activation

*Ying He,[a] Zhengpeng Yang,[a] Jiaguo Yu,[a] Difa Xu,[b] Chengyuan Liu,[c] Yang Pan,[c] Wojciech Macyk,[d] and Feiyan Xu[a,]**

[a] Laboratory of Solar Fuel, Faculty of Materials Science and Chemistry, China University of Geosciences, 68 Jincheng Street, Wuhan 430078, P. R. China

[b] Hunan Key Laboratory of Applied Environmental Photocatalysis, Changsha University, Changsha, 410022, P. R. China

[c] National synchrotron radiation laboratory, University of science and technology of China, Hefei, 230026, P. R. China

[d] Faculty of Chemistry, Jagiellonian University, ul. Gronostajowa 2, Kraków 30–387, Poland

* E-mail: xufeiyan@cug.edu.cn

1. Experimental section

1.1 Chemicals

Sodium tungstate dehydrate ($Na_2WO_4 \cdot 2H_2O$) and tetrafluoroboric acid (HBF_4, 40 wt.%) were obtained from Shanghai Aladdin biochemical technology Co., Ltd. Indium nitrate ($In(NO_3)_3 \cdot 4H_2O$) was purchased from Macklin Reagent Co., Ltd. All the chemicals were of analytical grade and used without further purification.

1.2 Characterizations

The X-Ray diffraction (XRD) patterns of as-obtained catalysts were recorded using a Shimadzu XRD-6100 X-ray diffractometer (Japan) with Cu *K*α radiation. Field emission scanning electron microscope (FESEM) images were characterized *via* JSM 7500F. Transmission electron microscopy (TEM), high-resolution transmission electron microscopy (HRTEM) and the corresponding energy-dispersive X-ray spectroscopy (EDX) mapping were studied by Talos F200S. The light absorption spectra of the prepared samples were obtained using a Shimadzu UV-2600 UV-visible spectrophotometer (Japan). The surface electronic states of the samples were determined by X-ray photoelectron spectroscopy (XPS) *via* a Thermo Scientific ESCALA 210 XPS spectrometer system (USA) with 300 W Al *K*α radiation. *In-situ* XPS measurements were performed under the same condition, except for the introduction of light irradiation. The binding energies were referenced to the C 1*s* peak at 284.8 eV from adventitious carbon. The contact potential difference (CPD) was recorded on a kelvin probe apparatus (Instytut Fotonowy, Poland).

And the work function of the probe is calibrated to be 4.25 eV by the gold tip as a standard reference surface. The carbon dioxide temperature-programmed desorption (CO_2-TPD) test was investigated on an BELCAT II (Microtrac MRB).

In-situ diffuse reflectance infrared Fourier transform spectroscopy (DRIFTS) were acquired on the Nicolet iS50 spectrometer (Thermo Scientific, USA). Time-resolved photoluminescence (TRPL) spectra were collected on a fluorescence lifetime spectrophotometer (FLS 1000, Edinburgh, UK) with an excitation wavelength of 375 nm. The average lifetime (τ_a) can be calculated according to the following equation:

$$\tau_a = \frac{A_1\tau_1^2 + A_2\tau_2^2 + A_3\tau_3^2}{A_1\tau_1 + A_2\tau_2 + A_3\tau_3} \quad (1)$$

where τ_1 represents the lifetime of radiative recombination process, τ_2 and τ_3 stand for the lifetime of non-radiative recombination and energy transfer process, respectively. A_1, A_2 and A_3 are the preexponential factors of decay curves.

Electrochemical measurements were conducted using a standard three-electrode system on an electrochemical workstation (CHI660C, China) in 50 mL of electrolyte containing 0.5 M Na_2SO_4. Pt wire (1.0 cm^2) and Ag/AgCl (filled with saturated KCl) were worked as the counter and reference electrodes, respectively. For the working electrode, a slurry was prepared by dispersing 20 mg of catalyst in 1.0 mL of ethanol and 10 μL of Nafion solution to make slurry, and then coated onto the conductive surface of FTO glasses with an active area of about 1.0 cm^2. The electrode was finally dried in an oven at 60 °C for 1 h.

1.3 Photocatalytic CO_2 reduction

The photocatalytic CO_2 reduction was carried out in an online gas-closed system equipped with a gas-circulated pump (OLPCRS-2, Shanghai Boyi Scientific Instrument Co., Ltd.). Typically, 50 mg of photocatalysts and 1 mL of H_2O were added in a Quartz and Pyrex glass hybrid reactor connecting to the CO_2 photoreduction system. The air-tight system was completely evacuated by using a vacuum pump, after which about 70 kPa of high-purity CO_2 (99.999%) gas was injected. Once achieving adsorption equilibrium, a 300 W Xe arc lamp with a 420 nm cut-off filter (Microsolar 300 Xenon lamp source, Beijing Perfectlight, China) was used as the light source. The photocatalytic CO_2 reduction products were analyzed using a gas chromatograph (GC-2030, Shimadzu Corp., Japan) equipped with barrier discharge ionization detector (BID) and a capillary column (Carboxen 1010 PLOT Capillary, 60 m × 0.53 mm). The apparent quantum efficiency (AQE) of the products over WI10 was calculated as follows:

$$\begin{aligned} \mathrm{AQE}(\%) &= \frac{\text{number of reacted electrons}}{\text{number of incident photons}} \times 100 \\ &= \frac{\text{number of CO molecules} \times 2 + \text{number of } CH_4 \text{ molecules} \times 8}{\text{number of incident photons}} \times 100 \\ &= \frac{(2 \times R_{CO} + 8 \times R_{CH4}) \times t_1 \times N_A}{P \times t_2 \times \frac{\lambda}{hc}} \times 100 \end{aligned} \quad (2)$$

where R_{CO} and R_{CH_4} are the CO and CH_4 production rate (mol h^{-1}); t_1 is the irradiation time (1 h); N_A is Avogadro constant (6.02 $\times 10^{23}$ mol^{-1}); P is the total incident light flux (W, J s^{-1}) and equals light intensity per unit area (E, W cm^{-2}) times effective irradiation area (S, cm^2), where E can be measured by the radiant power energy meter (UV-A and FZ-A, Photoelectric Instrument Factory of Beijing Normal University), S is 4.5 cm^2 in this

experiment; t_2 equals 3600 s; λ is the monochromatic light wavelength(m); h is the Planck constant (6.626×10^{-34} J s) and c is the light speed in vacuum (3×10^8 m s^{-1}).

Moreover, the selectivity of products was calculated by the following equation:

$$\text{selectivity of product } C_i(\%) = \frac{\text{yield rate of } C_i \ (\mu\text{mol h}^{-1})}{\text{total yield rates of all products}} \times 100 \qquad (3)$$

where C_i represents the reduction products including CO and CH_4.

Synchrotron-radiation vacuum ultraviolet photoionization mass spectrometry (SVUV-PIMS) was carried out at the combustion endstation of the BL03U beamline at the National Synchrotron Radiation Laboratory.

1.4 Computational details

The periodic DFT calculations were performed by using Vienna Ab-initio Simulation Package (VASP).[1] The exchange correlation between electrons was treated using the generalized gradient approximation (GGA) in the Perdew–Burke–Ernzerhof (PBE) form.[2-3] A (1×1) supercell of In_2O_3 (111) and a (2×2) supercell of WO_3 (001) surface slabs were adopted, where the half bottom atomic layers were fixed for all calculations. To avoid interactions between periodic structures, ~20 Å vacuum space was inserted. The cutoff energy was chosen at 520 eV, and the Brillouin zone was sampled using *k*-point spacing of 0.02 $Å^{-1}$.[4-6] The convergence thresholds for energy and atomic forces were set as 10^{-5} eV and 0.02 eV $Å^{-1}$, respectively. The van der Waals interaction between adsorbate and slab was corrected with the DFT-D3(BJ) method.[7-8]

The free energy (G) for each isolated or adsorbed molecule was calculated at 298.15 K with zero-point energy (ZPE) correction. The formula is $G = E + \mathrm{ZPE} - TS$, where E is the electronic energy calculated with VASP, ZPE is the zero-point energy and TS is the entropy contribution. The work function (Φ) of In_2O_3 (111) and WO_3 (001) slabs were calculated according to the formula of $\Phi = E_V - E_F$, where E_V and E_F stand for the vacuum energy level and Fermi level of the slabs, respectively.

2. Supporting Figures

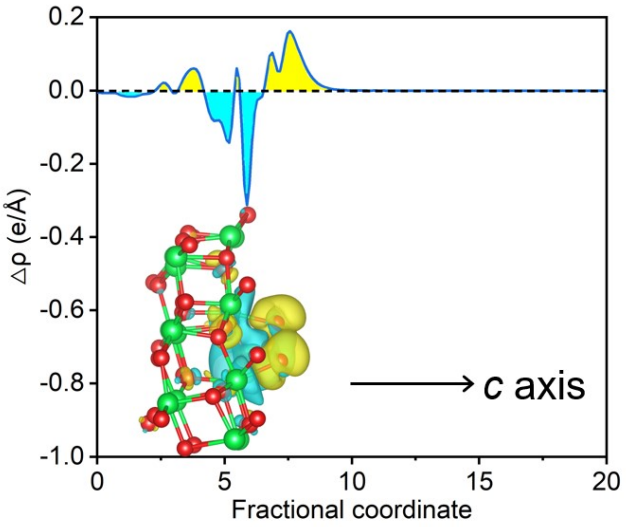

Fig. S1 Planar-averaged electron density difference $\Delta\rho$ of CO_2 absorbed on In_2O_3. Cyan and yellow areas indicate electron depletion and accumulation, respectively.

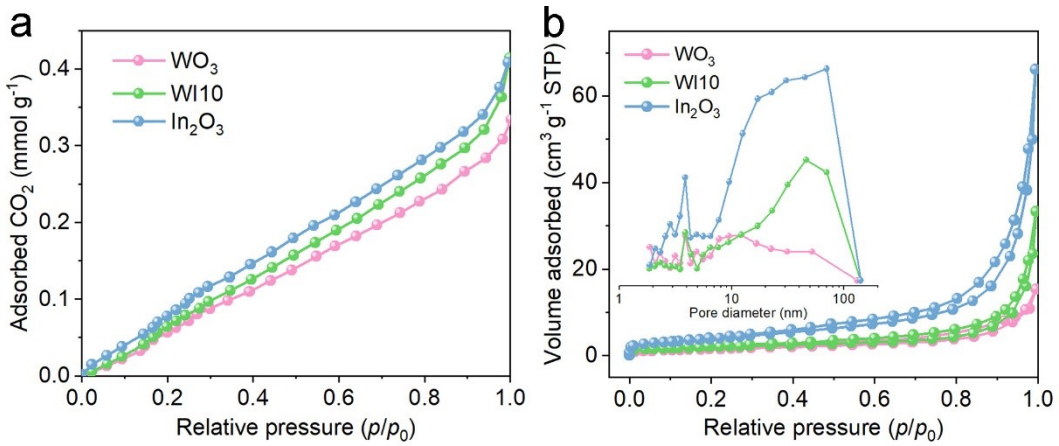

Fig. S2 (a) CO_2 adsorption isotherms, (b) nitrogen adsorption-desorption isotherms and the corresponding pore size distribution (inset) of WO_3, WI10 and In_2O_3. WI10 represents the WO_3/In_2O_3 heterojunctions, where W and I represent WO_3 and In_2O_3, respectively; *10* is the molar ratios of In_2O_3 in WO_3/In_2O_3 composites.

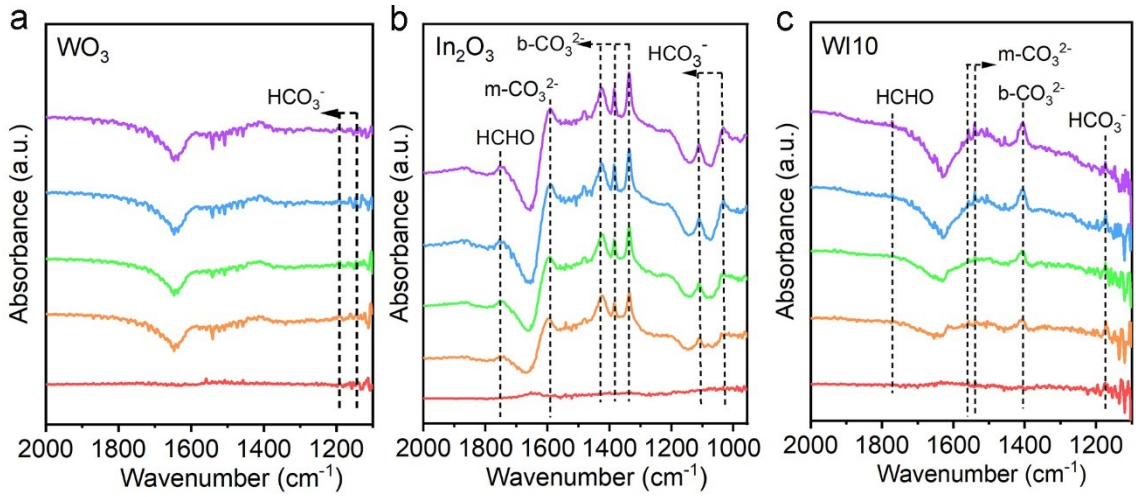

Fig. S3 *In-situ* DRIFT spectra of (a) WO_3, (b) In_2O_3 and (c) WI10 after adsorption of CO_2 for 15, 30, 45 and 60 min in dark. WI10 represents the WO_3/In_2O_3 heterojunctions, where W and I represent WO_3 and In_2O_3, respectively; *10* is the molar ratios of In_2O_3 in WO_3/In_2O_3 composites.

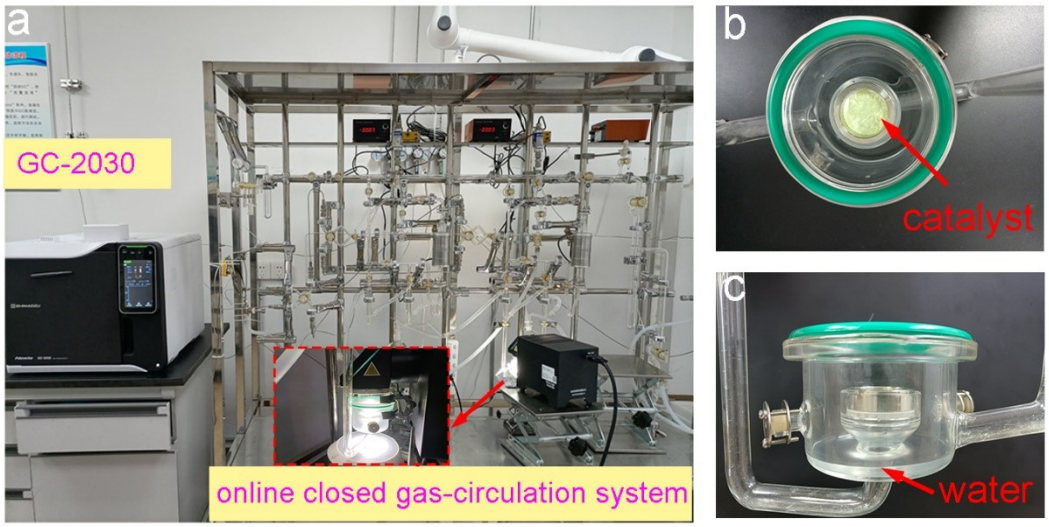

Fig. S4 (a) The online closed gas-circulation system and (b) the quartz reactor for photocatalytic CO_2 reduction.

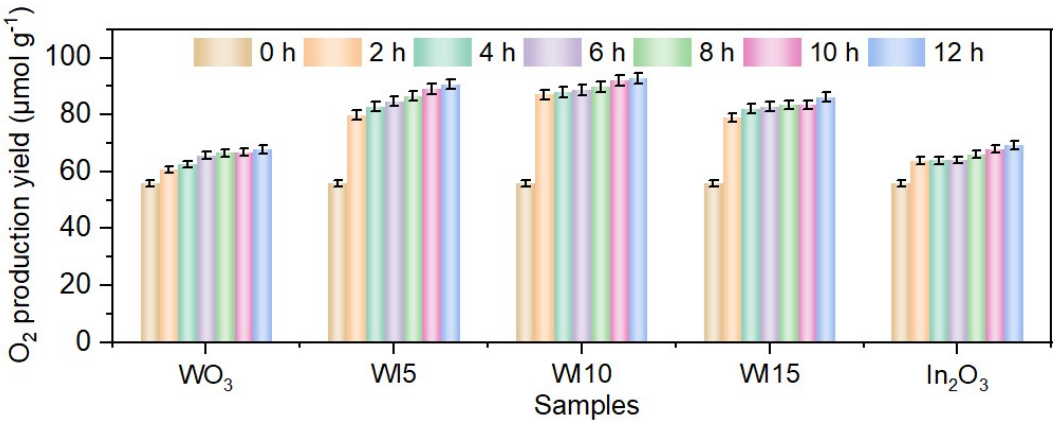

Fig. S5 O_2 production yield over WO_3, WI*x*, and In_2O_3 during 12-h experiment performed under visible light irradiation. The initial O_2 comes from the input high-purity CO_2 (99.999%), and its concentrations were normalized. WI*x* represents the WO_3/In_2O_3 heterojunctions, where W and I represent WO_3 and In_2O_3, respectively; *x* is the molar ratios of In_2O_3 in WO_3/In_2O_3 composites.

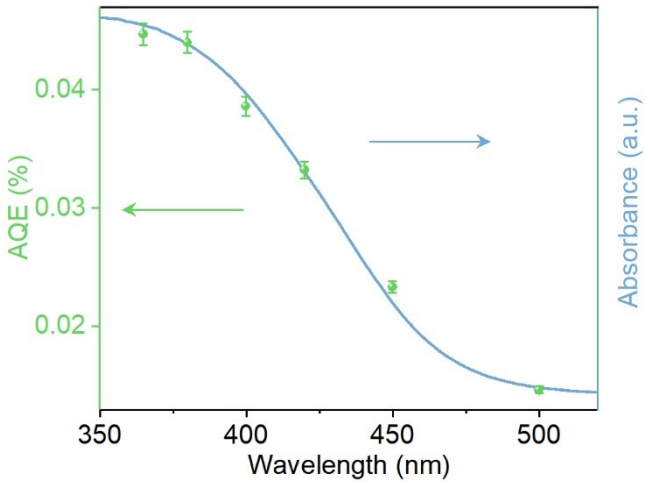

Fig. S6 Wavelength-dependent AQE and the UV-vis absorption spectrum of WI10 sample. WI10 represents the WO_3/In_2O_3 heterojunctions, where W and I represent WO_3 and In_2O_3, respectively; *10* is the molar ratios of In_2O_3 in WO_3/In_2O_3 composites.

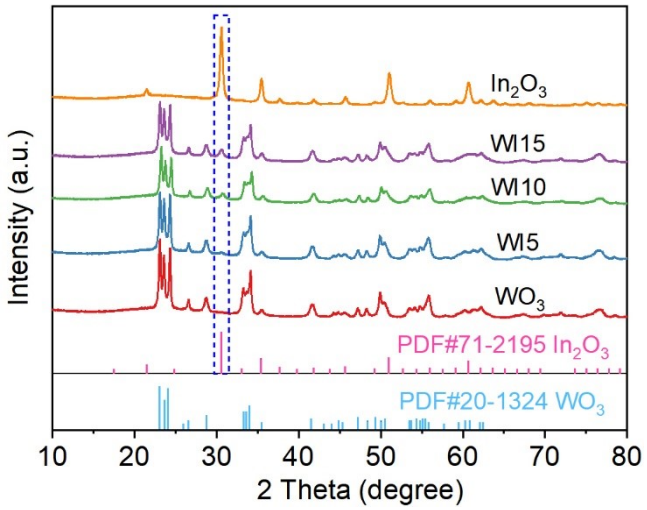

Fig. S7 XRD patterns of WO_3, In_2O_3 and WI*x*. WI*x* represents the WO_3/In_2O_3 heterojunctions, where W and I represent WO_3 and In_2O_3, respectively; *x* is the molar ratios of In_2O_3 in WO_3/In_2O_3 composites.

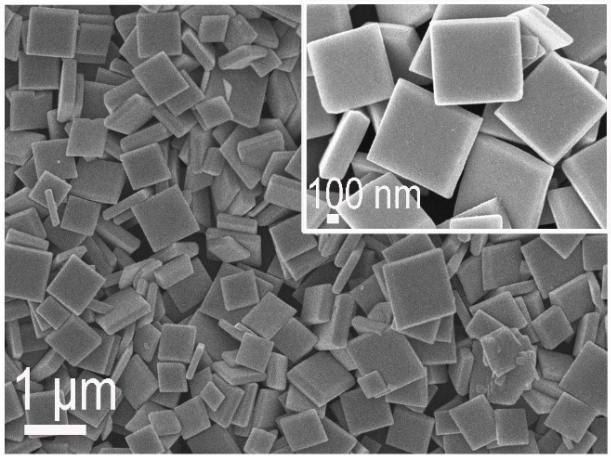

Fig. S8 FESEM image of precursor $WO_3 \cdot H_2O$.

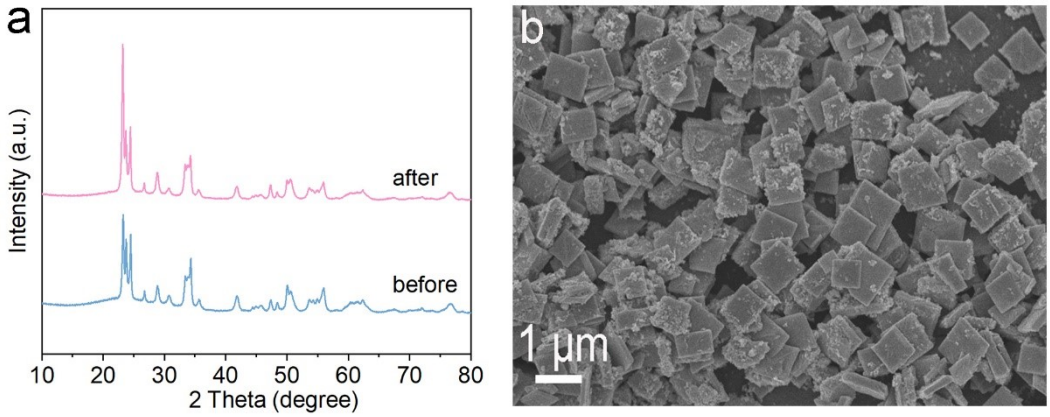

Fig. S9 (a) XRD pattern and (b) FESEM image of WI10 after photocatalytic reactions. WI10 represents the WO_3/In_2O_3 heterojunctions, where W and I represent WO_3 and In_2O_3, respectively; *10* is the molar ratios of In_2O_3 in WO_3/In_2O_3 composites.

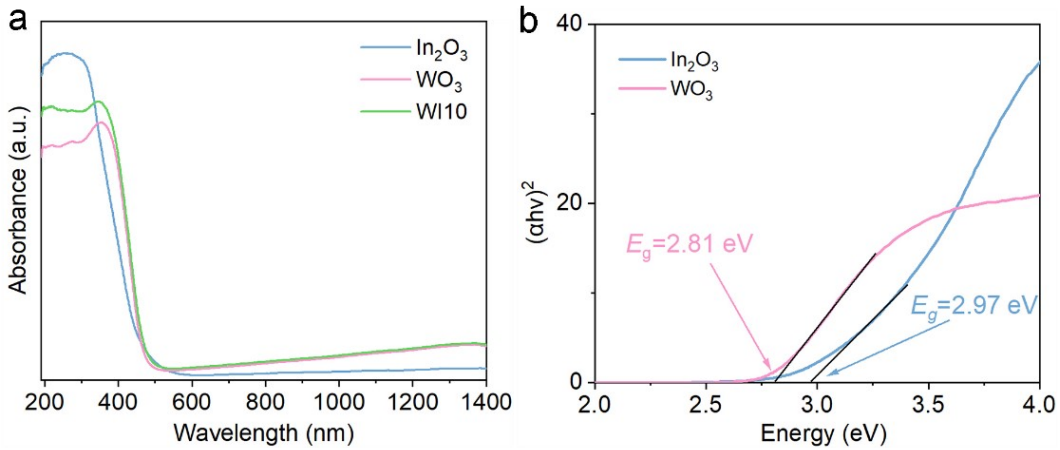

Fig. S10 (a) UV-vis spectra of WO_3, In_2O_3 and WI10, (b) Kubelka-Munk plots of WO_3 and In_2O_3. WI10 represents the WO_3/In_2O_3 heterojunctions, where W and I represent WO_3 and In_2O_3, respectively; *10* indicates the molar ratios of In_2O_3 in WO_3/In_2O_3 composites.

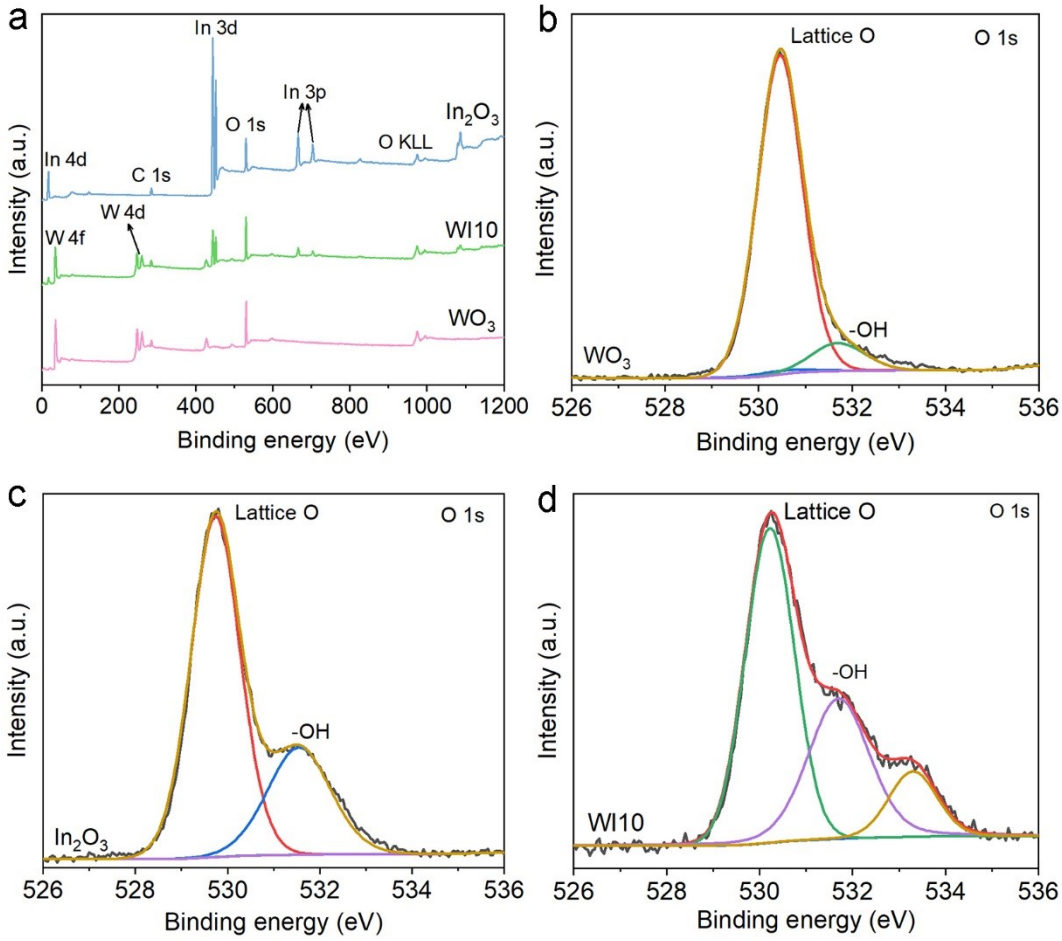

Fig. S11 (a) XPS survey spectra, XPS spectra of O 1*s* of (b) WO_3, (c) In_2O_3, and (d) WI10. WI10 represents the WO_3/In_2O_3 heterojunctions, where W and I represent WO_3 and In_2O_3, respectively; *10* indicates the molar ratios of In_2O_3 in WO_3/In_2O_3 composites.

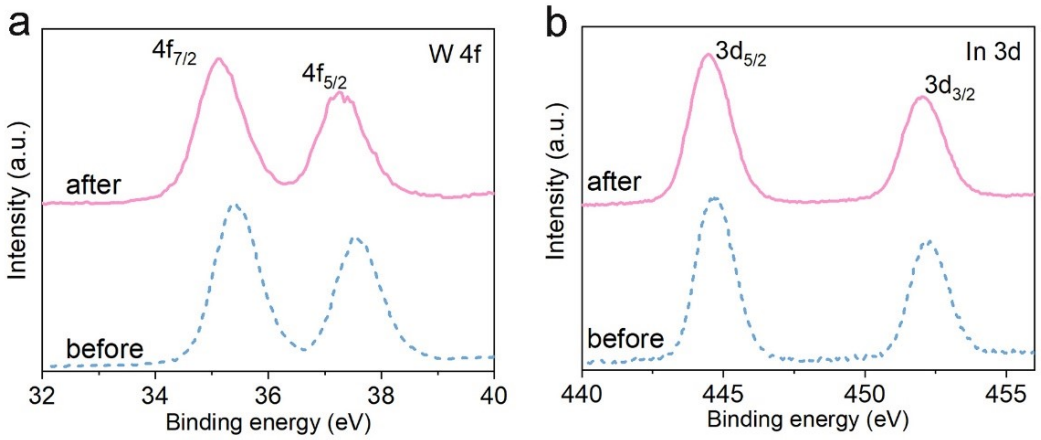

Fig. S12 XPS spectra of (a) W 4*f* and (b) In 3*d* of WI10 before and after photocatalytic reactions. WI10 represents the WO_3/In_2O_3 heterojunctions, where W and I represent WO_3 and In_2O_3, respectively; *10* is the molar ratios of In_2O_3 in WO_3/In_2O_3 composites.

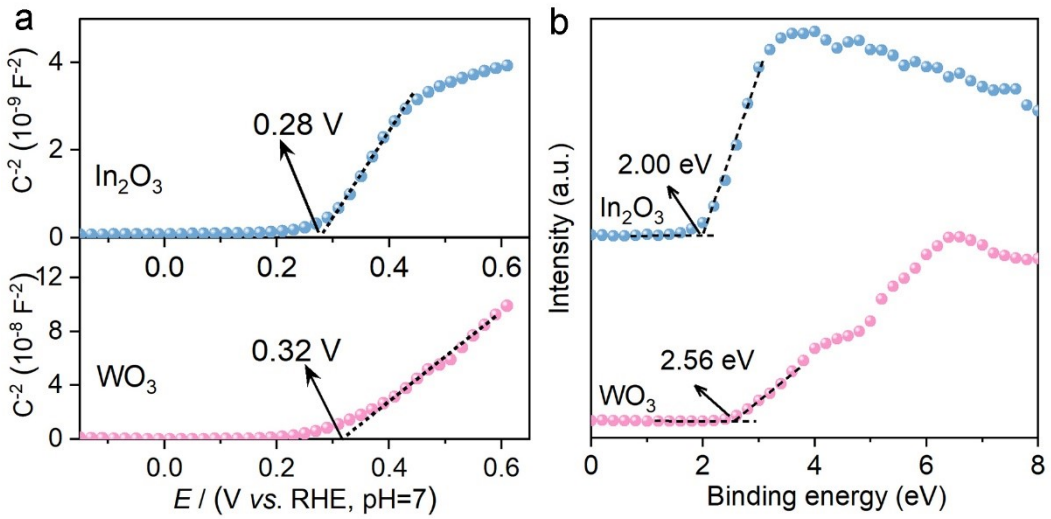

Fig. S13 (a) Mott–Schottky plots and (b) valence band XPS spectra of WO_3 and In_2O_3.

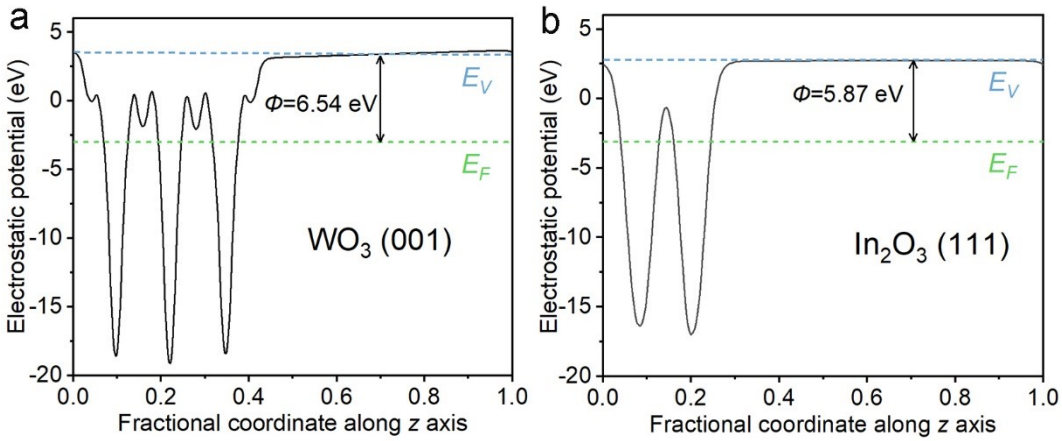

Fig. S14 Calculated electrostatic potentials of (a) WO_3 (001) and (b) In_2O_3 (111) slabs.

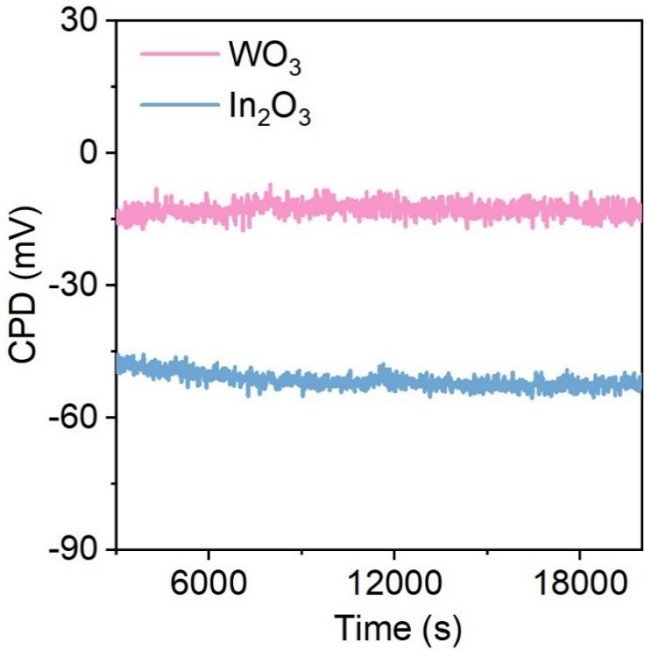

Fig. S15 CPD profile of WO_3 and In_2O_3 in the dark.

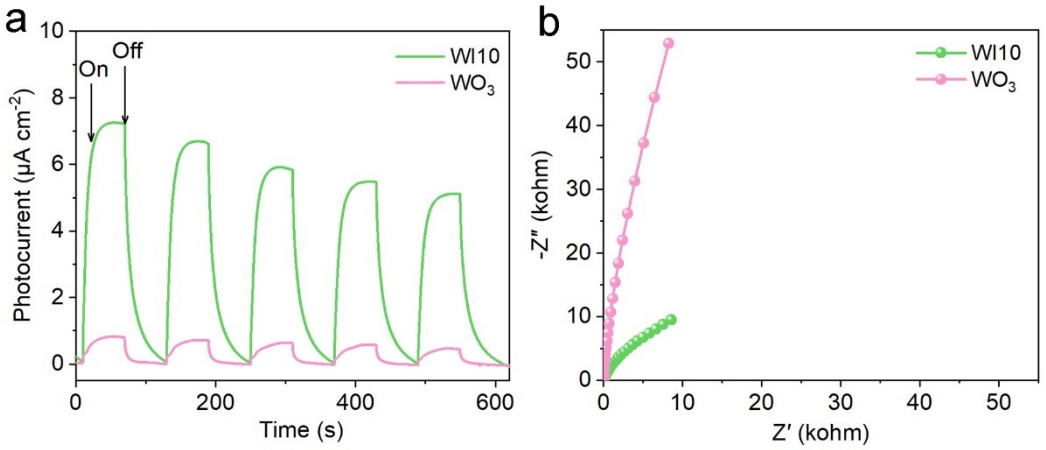

Fig. S16 (a) Transient photocurrent response and (b) Nyquist plots of WO_3 and WI10. WI10 represents the WO_3/In_2O_3 heterojunctions, where W and I represent WO_3 and In_2O_3, respectively; *10* indicates the molar ratios of In_2O_3 in WO_3/In_2O_3 composites.

3. Supporting Tables

Table S1. Physical properties of WO_3, WI10 and In_2O_3. WI10 represents the WO_3/In_2O_3 heterojunctions, where W and I represent WO_3 and In_2O_3, respectively; *10* is the molar ratios of In_2O_3 in WO_3/In_2O_3 composites.

Sample	S_{BET} (m^2/g)	V_p (cm^3/g)	d_p (nm)
WO_3	6	0	15.2
WI10	7	0.1	23.8
In_2O_3	15	0.1	24.7

Table S2. The calculated AQE at different monochromatic wavelengths over the WI10 sample. WI10 represents the WO_3/In_2O_3 heterojunctions, where W and I represent WO_3 and In_2O_3, respectively; *10* is the molar ratios of In_2O_3 in WO_3/In_2O_3 composites.

λ (nm)	365	380	400	420	450	500
E (mW/cm^2)	14	15	17	14	20	12
M_{CO} (ppm)	7.71	3.56	4.21	3.72	3.47	0.00
R_{CO} (μmol/h)	0.0026	0.0012	0.0014	0.0013	0.0012	0.0000
M_{CH_4}(ppm)	3.75	5.35	5.48	3.93	4.35	2.18
R_{CH_4}(μmol/h)	0.0013	0.0018	0.0019	0.0013	0.0015	0.0007
AQE (%)	0.0447	0.0440	0.0386	0.0332	0.0233	0.0146

Table S3. The fitted lifetimes obtained from decay curves of WO_3 and WI10 in different atmospheres. WI10 represents the WO_3/In_2O_3 heterojunctions, where W and I represent WO_3 and In_2O_3, respectively; *10* is the molar ratios of In_2O_3 in WO_3/In_2O_3 composites.

Sample	τ_1 (ns)	τ_2 (ns)	τ_3 (ns)	τ_a (ns)
WO_3-Ar	0.96	3.44	9.35	4.15
WI10-Ar	0.76	2.98	8.83	3.56
WI10-CO_2	0.71	3.05	9.03	3.38

References

1. K. Lejaeghere, V. Van Speybroeck, G. Van Oost, S. Cottenier, *Crit. Rev. Solid State Mater. Sci.*, 2014, **39**, 1-24.
2. X. Tao, P. Pan, T. B. Huang, L. Chen, H. D. Ji, J. J. Qi, F. B. Sun, W. Liu, *Chem. Eng. J.*, 2020, **395**, 125186.
3. Y. Peng, W. Z. Si, X. Li, J. M. Luo, J. H. Li, J. Crittenden, J. M. Hao, *Appl. Catal. B*, 2016, **181**, 692-698.
4. D. Z. Zhang, Y. H. Cao, Z. M. Yang, J. F. Wu, *ACS Appl. Mater. Interfaces*, 2020, **12**, 11979-11989.
5. J. Y. Ye, C. J. Liu, D. H. Mei, Q. F. Ge, *ACS Catal.*, 2013, **3**, 1296-1306.
6. L. F. Song, K. P. Dou, R. R. Wang, P. Leng, L. Q. Luo, Y. Xi, C. C. Kaun, N. Han, F. Y. Wang, Y. F. Chen, *ACS Appl. Mater. Interfaces*, 2020, **12**, 1270-1279.
7. B. C. Zhu, B. Cheng, L. Y. Zhang, J. G. Yu, *Carbon Energy*, 2019, **1**, 32-56.
8. I. B. Obot, D. D. Macdonald, Z. M. Gasem, *Corros. Sci.*, 2015, **99**, 1-30.